Published in final edited form as:
IEEE Trans Ultrason Ferroelectr Freq Control. 2012 July ; 59(7): 1602–1608. doi:10.1109/TUFFC.2012.2360.

Assessing and improving acoustic radiation force image quality using a 1.5D transducer design

Ali .H. Dhanaliwala, **John A. Hossack**, and **F. William Mauldin Jr.**
Department of Biomedical Engineering, University of Viriginia, Charlottesville, VA

F. William Mauldin: fwm5f@virginia.edu

Abstract

A 1.5D transducer array was developed to improve acoustic radiation force impulse (ARFI) imaging signal-to-noise ratio (SNR_{ARFI}) and image contrast relative to a conventional 1D array. To predict performance gains from the proposed 1.5D transducer array, an analytical model for SNR_{ARFI} upper bound was derived. The analytical model and 1.5D ARFI array were validated using a finite element model-based numerical simulation framework. The analytical model demonstrated good agreement with numerical results (correlation coefficient = 0.995), and simulated lesion images yielded a significant (2.92 dB; $p < 0.001$) improvement in contrast-to-noise ratio when rendered using the 1.5D ARFI array.

Keywords

Acoustic Radiation Force Impulse Imaging; ARFI; Echo Decorrelation; 1.5D Array

Introduction

Acoustic radiation force imaging is a classification of ultrasound imaging that uses tissue displacement, rather than acoustic reflectivity, as the source of image contrast. In general, these techniques produce images by using acoustic radiation force to push tissue, followed by a series of tracking pulses to measure displacement. This displacement can then be used to calculate relative or absolute stiffness. Radiation force imaging techniques, such as acoustic radiation force impulse (ARFI) imaging [1], shear wave imaging [2–7], and monitored steady-state excitation and recovery imaging [8], have shown promise in detecting lesions in a variety of organs including the abdomen [9], [10], heart [11], liver [12], breast [13], and prostate [15] as well as measuring blood coagulation *ex vivo* [16], [17]. Since contrast is derived from stiffness, and stiffness is derived from displacement, the mean and variance of the displacement estimates have a large impact on lesion detection.

A major limiting factor in displacement estimation performance during ARFI imaging is echo decorrelation. While larger acoustic output, and thus larger acoustic radiation force, can increase ARFI image signal (*i.e.* displacement magnitude), displacement variance is also increased due to echo decorrelation from increased scatterer shearing [18], [19]. Additionally, increasing displacement magnitude is further limited by tissue ultrasound absorption and heating considerations (e.g. < 15 μm for < 1°C tissue heating [20]). In addition to increasing displacement variance, decorrelation derived from scatterer shearing

is also associated with an underestimation of the peak displacement magnitude [19]. Therefore, displacement estimate improvements (*i.e.* high mean displacements and lower variance) are strongly dependent on the ability to reduce decorrelation between the reference and subsequent tracking echo signals. While signal processing methods, including principle component analysis [21], [22], can reduce decorrelation, it is also recognized that transducer design and imaging parameters effect the degree of differential motion across the point spread function, and thus, the observed levels of echo decorrelation [18]. In this paper, a new 1.5D ARFI transducer design is proposed for reduced echo decorrelation, and improved ARFI image signal-to-noise ratio (SNR_{ARFI}), compared with a conventional 1D array. Echo decorrelation improvements are achieved using the 1.5D design because it enables electronic focusing in elevation and dedicated elements for each of the pushing and tracking functions. To investigate the relationship between echo decorrelation, transducer design, and image quality, we first develop an analytical model that relates the properties of a transducer to a radiation force image quality metric, SNR_{ARFI}. While we focus on ARFI imaging, this analysis can be generalized to any radiation force imaging technique that share the common feature of deriving image contrast from displacement estimates. Using this new analytical model, an upper bound for SNR_{ARFI} is derived as a function of tissue properties, transducer geometry, and imaging parameters. This model is validated using a numerical simulation framework and used, along with finite element model (FEM) simulations, to assess the performance of the proposed 1.5D array design compared with a convention 1D array in terms of SNR_{ARFI} and contrast-to-noise ratio.

II Theory and Methods

A. Derivation of ARFI Image SNR upper bound

Image contrast in ARFI imaging is derived from differences in tissue stiffness, which are manifest in different displacement responses assuming constant acoustic radiation force excitation – *i.e.* assuming constant attenuation and tissue within a small distance of the transmit focus. With application of the same acoustic radiation force, stiffer tissue exhibits less displacement than more compliant tissue. Images are typically formed as maps of displacement estimates computed from locations within the 2D imaging region. To quantify image quality and assess the performance of the proposed 1.5D ARFI transducer design (described further below), an upper bound for SNR_{ARFI} was derived. We start by defining SNR_{ARFI} as follows:

$$SNR_{ARFI}=\frac{\mu}{\sigma} \quad (1)$$

where μ and σ are the mean and standard deviation (or "jitter") of the estimated displacement, respectively. The standard deviation of ultrasound motion estimation depends on electronic signal-to-noise (SNR_E), echo correlation (ρ), center frequency (f_o), motion estimator window length (T), and fractional bandwidth (B). An expression for the minimum jitter ($\hat{\sigma}$) achievable from an unbiased time delay estimator was previously derived by Walker and Trahey [23]:

$$\hat{\sigma} \geq \sqrt{\frac{3}{2f_0^3\pi^2T(B^3+12B)}\left(\frac{1}{\rho^2}\left(1+\frac{1}{SNR_E^2}\right)^2-1\right)} \quad (2)$$

While there are several parameters in (2), echo correlation is an important factor dictating estimator performance since small increments result in large gains [23]. Under typical imaging conditions – 30 dB SNR_E and 80% BW – improving ρ by just 0.009, from 0.99 to 0.999, reduces jitter by 64%.

The physical source of decorrelation (1-ρ) between successive echoes result from either of two phenomena – out of beam motion or differential motion across the point spread function [21]. Both phenomena result in shifted and decorrelated versions of the reference echo, rather than perfectly shifted replicas, following displacement. As a result, bias and variance of the displacement estimate increase. Out of beam decorrelation typically occurs when scatterers move into and out of the point spread function between subsequent received echoes and is most common in imaging techniques with large displacements (*e.g.* elastography or Doppler) or in regions of the anatomy exhibiting large physiological motion (*e.g.* cardiac imaging). Differential motion decorrelation occurs when scatterers are differentially displaced within the pushing beam. Since displacements in ARFI and other radiation force imaging techniques are small (~10 μm [24]), the contribution of out of beam motion to decorrelation is often viewed as insignificant and ignored in further theoretical or FEM analysis [18], [19], [25], [26]. However, as evidenced by the work of several groups to implement physiological motion filters [11], [27], [28], out of beam motion in ARFI imaging can occur due to physiological motion. Nevertheless, the present work continues as in previous work with contributions from out of beam decorrelation assumed to be negligible. This assumption is valid in nearly all physiological environments with the exceptions of cardiac imaging. Even in this environment, the source of out of beam decorrelation (*i.e.* cardiac motion) occurs on a time scale that is slower than the source of differential motion decorrelation (*i.e.* radiation force-induced displacements).

McAleavey *et al* [18] derived an expression for the magnitude of differential motion decorrelation in ARFI imaging that is a function of motion amplitude and the ratio of pushing beam width to tracking beam width. A major assumption of this derivation is that tissue displacement width is equal to the width of the two way response of the pushing beam and that displacement only occurs in the axial direction. Tissue, and other linearly elastic materials, however, exhibit mechanical coupling effects that result in tissue displacement widths that are wider than the pushing beam width and occur in all three directions (Fig 1b) [25], [29]. To correct for this effect, echo correlation is described using the expression from McAleavey [18], but accounting for mechanical coupling through parameters, L_X and L_Y:

$$\rho=1-\frac{1}{c^2}4A^2f_0^2\pi^2L_xL_y\left(\frac{1}{\sqrt{(1+L_x^2)(1+L_y^2)}}-\frac{4L_xL_y}{(1+2L_x^2)(1+2L_y^2)}\right) \quad (3)$$

$$L_x=\frac{D_x}{T_x},\ L_y=\frac{D_y}{T_y} \quad (4)$$

where A is the maximum scatterer displacement, c is the speed of sound, and D_x, T_x, D_y, T_y, are displacement and tracking beam widths in the lateral and elevational dimensions, respectively. The parameters relating displacement to tracking beam widths in (3) and (4), L_X and L_Y, replace the W_X and W_Y parameters relating pushing to tracking beam widths from McAleavey [18]. Substituting (3) into (2) results in a new expression for the jitter lower bound in ARFI imaging:

$$\hat{\sigma} \geq \sqrt{\frac{3}{2f_0^3\pi^2T(B^3+12B)}\left(\frac{1}{\left(1-\frac{1}{c^2}4A^2f_0^2\pi^2L_xL_y\left(\frac{1}{\sqrt{(1+L_x^2)(1+L_y^2)}}-\frac{4L_xL_y}{(1+2L_x^2)(1+2L_y^2)}\right)\right)^2}\left(1+\frac{1}{SNR_E^2}\right)^2-1\right)} \quad (5)$$

where $\hat{\sigma}$ is in units of seconds. McAleavey *et al* [18] further derived an expression for ARFI imaging signal (*i.e.* the expectation value of the displacement estimate). Replacing the assumption of equal displacement and pushing beam widths with the updated expression in (4) results in a new expression for ARFI image signal:

$$\mu=\frac{2AWL_xL_y}{\sqrt{(2L_x^2+1)\left(2L_y^2+1\right)}} \quad (6)$$

Substituting (5) and (6) into (1) and scaling by c/2 to maintain consistent units results in a final expression for the upper bound of SNR_{ARFI}:

$$\hat{SNR}_{ARFI} \leq \frac{\mu}{\left(\hat{\sigma}\frac{c}{2}\right)} \quad (7)$$

The upper bound in (7) results in larger SNR_{ARFI} values when compared with an upper bound derived using McAleavey's pushing beam width as a proxy for displacement width (Fig 1).

B. Numerical Simulation Framework

A numerical simulation framework (Fig 1a) was developed based on previously described FEM simulation methods [19], [25], [26] to validate the derived analytical model in (7). Transducer design and relevant imaging parameters were selected and the intensity field was calculated using FIELD II [30]. Since intensity is proportional to the acoustic radiation force [31], [32], FIELD II results provided the body force input parameters for the FEM (COMSOL Multiphysics, COMSOL Inc. Burlington MA) simulations. FEM simulations were performed using a 50 mm × 50 mm × 50 mm block and a free tetrahedral mesh. Mesh element size was optimized to adequately sample displacement while minimizing the total number of elements. A maximum element size of 0.5 mm was used in regions where displacement estimates were extracted. To mimic human tissue using linear elastic

assumptions, a Poisson's ratio (ν) of 0.49 [1] was used. Three-dimensional displacement fields were calculated from FEM simulations using a linear GMRES (generalized minimal residual) iterative solver [33] and a geometric multigrid preconditioner [34]. The displacement results were then imported into MATLAB and scaled to achieve the desired peak displacement value. FEM simulations were conducted using static analysis where displacement fields represented immediate deformation responses to an impulsive acoustic radiation force. This time point is of greatest interest in ARFI imaging as images are typically formed using the maximum displacement parameter. Additionally, it is this time point where the proposed 1.5D array is anticipated to make the greatest contribution as later time points yield less differential motion decorrelation due to lower displacements and shear wave propagation [19]. Using these FEM methods, the mechanical coupling effects were incorporated into the proposed analytical model, D_X and D_Y described above, by measuring the lateral FWHM displacement at the focus.

Received echo data from the proposed transducer array were simulated by first building a 20 mm × 40 mm × 25 mm volume comprising 2.5×10^5 uniformly distributed point scatterers with Gaussian distributed amplitudes. Reference, pre-motion, echoes were calculated using the FIELD II function calc_scat. A second echo, representing received echo data from the ARFI "tracking" pulse, was then simulated by displacing scatterers according to the FEM displacement field results and then repeating the calc_scat computation. Electronic noise was modeled as additive Gaussian white noise. Displacements were calculated using the Loupas autocorrelation method [35] and a sliding window length of 1.5 periods of the tracking center frequency.

SNR_{ARFI} was calculated from displacement results as the ratio of the sample mean to the standard deviation of the calculated displacement. Mean and standard deviation for SNR_{ARFI} values were computed by repeating the simulation over multiple (n = 30) independent realizations of scatterer positions, amplitudes, and electronic noise.

C. 1.5D ARFI Transducer Design and Comparison

A 1.5D transducer array for ARFI imaging was designed for the purpose of increasing SNR_{ARFI} using insights from the analytical model, while taking hardware complexity into consideration (*i.e.* 1.5D is less complex than a 1.75D or 2D array solution). SNR_{ARFI} improvements using the 1.5D array is derived from mitigation of echo decorrelation through two primary mechanisms. First, the additional rows of elements enable electronic focusing in elevation, thus reducing the tracking beam width in this dimension. Second, the functions of pushing and tracking pulses can be assigned to different rows (Fig 2). This allows pushing rows to use lower frequency elements than the tracking rows, thus widening the pushing beam width relative to the tracking beam width. The parameters describing the 1.5D array and a conventional 1D array are given in Table I.

SNR_{ARFI} for the 1.5D ARFI array and a conventional 1D array were computed over a range of peak displacements, using the numerical framework outlined above. In addition, a 4 mm diameter soft lesion [36] at a depth of 20 mm within a stiffer homogeneous background tissue, representing breast tissue [37], was simulated. All parameters were the same as above except the maximum element size of the tissue block, transducer focal area, and lesion were

2 mm, 0.5 mm, and 0.25 mm, respectively. Images of the lesion produced with the 1.5D ARFI or the conventional 1D array were produced. Elastic modulus contrast between the simulated lesion and background tissue was 1:10 (*e.g.* 10 kPa lesion in a 100 kPa background) with peak displacement inside the lesion of 12 μm. Image contrast-to-noise ratio (CNR) was calculated as [38]:

$$CNR = 20\log_{10}\left(\frac{|\mu_i - \mu_o|}{\sigma_o}\right) \quad (8)$$

on median filtered images, where μ_i and μ_o are the mean displacements within equal area regions inside and outside the lesion, respectively, and σ_o is the standard deviation of displacement outside the lesion.

III. Results and Discussion

To validate the analytical model (7), SNR_{ARFI} was calculated for independent realizations of scatterers with increasing peak displacement for both the conventional 1D array and 1.5D ARFI array (Fig 3). The solid lines denote the derived SNR_{ARFI} upper bound and the symbols represent numerical simulation results. Excellent agreement was observed between numerical simulation results and the proposed SNR_{ARFI} analytical upper bounds – correlation coefficients of 0.995 and 0.998 for the 1D and 1.5D arrays respectively. In addition, the 1.5D ARFI array had an increased SNR_{ARFI} for all normalized displacements as compared to the 1D array ($p < 0.05$). Finally, when SNR_{ARFI} was calculated for increasing SNR_E, it was found to plateau above 30 dB. This trend substantiates the importance of improving SNR_{ARFI} through reductions in echo decorrelation as corresponding SNR_{ARFI} gains achieved via higher SNR_E are negligible.

Pushing and tracking beam widths for the conventional 1D and 1.5D ARFI imaging arrays were calculated using FIELD II (Table II). By enabling electronic focusing in the elevational dimension, the 1.5D ARFI array possessed a significantly wider pushing beam and narrower tracking beam width as compared to the conventional 1D array. Additionally, due to an ability to use dedicated elements for pushing and tracking functions, different center frequency ceramics were used for different rows of the 1.5D array (*e.g.* 2 MHz and 7 MHz for the 1.5 D array versus 4.21 MHz and 6.15 MHz for the conventional 1 D array as described in Table I). Thus, while more substantial gains in displacement to tracking beam widths were observed in the elevational dimension, gains were also achieved in the lateral dimension due to a larger range of center frequencies.

Lesion simulations were performed with independent realizations of scatterers for the purpose of illustrating the effects of transducer geometries and parameters on image quality (Fig 4). The lesion was better delineated – a 2.92 dB improvement (two-sided t-test, $p < 0.0001$) – when imaged using the 1.5D ARFI array over the conventional 1D array (Table III).

IV. Conclusion

An analytical model for the upper bound of ARFI image SNR, a metric for comparing ARFI image quality, has been derived as a function of tissue properties, imaging parameters, and transducer geometry. The analytical model was validated using a numerical simulation framework that coupled FIELD II to a finite element tissue model. By accounting for tissue displacement, there was excellent agreement between the analytical model and the numerical simulations. Using insight gained from the analytical model, a novel 1.5D array for ARFI imaging was designed. The 1.5D ARFI array increased displacement to tracking beam width ratio by allowing electronic focusing in the elevation and by allowing the pushing elements to be at a lower center frequency than the tracking elements. These improvements, impossible in a 1D array, resulted in an overall increase in echo correlation and improved SNR_{ARFI} as predicted by the analytical model. When compared to a conventional 1D array, the 1.5D ARFI array provided significantly improved displacement estimation, ARFI image SNR, and image CNR. Finally, the coupling of transducer design to an accurate analytical model of ARFI image SNR highlights the potential utility of this new tool. By using the analytical model to develop more sophisticated transducers that improve image quality, the clinical utility of ARFI can be improved for more accurate assessments of tissue material properties or better delineation of different tissue structures, such as lesions or arterial plaques.

References

1. Nightingale KR, Palmeri ML, Nightingale RW, Trahey GE. On the feasibility of remote palpation using acoustic radiation force. J Acoust Soc Am. Jul; 2001 110(1):625–634. [PubMed: 11508987]
2. Sarvazyan AP, Rudenko OV, Swanson SD, Fowlkes JB, Emelianov SY. Shear wave elasticity imaging: a new ultrasonic technology of medical diagnostics. Ultrasound Med Biol. Nov; 1998 24(9):1419–1435. [PubMed: 10385964]
3. Chen S, Fatemi M, Greenleaf JF. Quantifying elasticity and viscosity from measurement of shear wave speed dispersion. J Acoust Soc Am. Jun; 2004 115(6):2781–2785. [PubMed: 15237800]
4. Bercoff J, Tanter M, Fink M. Supersonic shear imaging: a new technique for soft tissue elasticity mapping. IEEE Trans Ultrason Ferroelectr Freq Control. Apr; 2004 51(4):396–409. [PubMed: 15139541]
5. McAleavey SA, Menon M, Orszulak J. Shear-modulus estimation by application of spatially-modulated impulsive acoustic radiation force. Ultrason Imaging. Apr; 2007 29(2):87–104. [PubMed: 17679324]
6. Fink M, Tanter M. Multiwave imaging and super resolution. Phys Today. 2010; 63(2):28.
7. Bavu E, Gennisson JL, Mallet V, Osmanski BF, Couade M, Bercoff J, Fink M, Sogni P, Vallet-Pichard A, Nalpas B. 406 Supersonic Shear Imaging is a New Potent Morphological Non-Invasive Technique to Assess Liver Fibrosis. Part I: Technical Feasibility. Journal of Hepatology. Apr.2010 52:S166–S166.
8. Mauldin FW, Haider MA, Loboa EG, Behler RH, Euliss LE, Pfeiler TW, Gallippi CM. Monitored steady-state excitation and recovery (MSSER) radiation force imaging using viscoelastic models. IEEE Trans Ultrason Ferroelectr Freq Control. Jul; 2008 55(7):1597–1610. [PubMed: 18986950]
9. Fahey BJ, Nelson RC, Bradway DP, Hsu SJ, Dumont DM, Trahey GE. In vivo visualization of abdominal malignancies with acoustic radiation force elastography. Phys Med Biol. Jan; 2008 53(1):279–293. [PubMed: 18182703]
10. Fahey B, Nightingale K, Nelson R, Palmeri M, Trahey G. Acoustic radiation force impulse imaging of the abdomen: demonstration of feasibility and utility. Ultrasound in Medicine & Biology. Sep; 2005 31(9):1185–1198. [PubMed: 16176786]

11. Hsu SJ, Bouchard RR, Dumont DM, Wolf PD, Trahey GE. In vivo assessment of myocardial stiffness with acoustic radiation force impulse imaging. Ultrasound Med Biol. Nov; 2007 33(11): 1706–1719. [PubMed: 17698282]
12. Palmeri ML, Wang MH, Dahl JJ, Frinkley KD, Nightingale KR. Quantifying hepatic shear modulus in vivo using acoustic radiation force. Ultrasound Med Biol. Apr; 2008 34(4):546–558. [PubMed: 18222031]
13. Sharma, AC.; Soo, MS.; Trahey, GE.; Nightingale, KR. Acoustic radiation force impulse imaging of in vivo breast masses. IEEE Ultrasonics Symposium; 2004; Montreal, Canada. p. 728-731.
15. Zhai L, Madden J, Foo WC, Palmeri ML, Mouraviev V, Polascik TJ, Nightingale KR. Acoustic radiation force impulse imaging of human prostates ex vivo. Ultrasound Med Biol. Apr; 2010 36(4):576–588. [PubMed: 20350685]
16. Hartley CJ. Characteristics of acoustic streaming created and measured by pulsed Doppler ultrasound. IEEE Trans Ultrason, Ferroelect, Freq Contr. Nov; 1997 44(6):1278–1285.
17. Mauldin FW, Viola F, Hamer TC, Ahmed EM, Crawford SB, Haverstick DM, Lawrence MB, Walker WF. Adaptive force sonorheometry for assessment of whole blood coagulation. Clin Chim Acta. May; 2010 411(9–10):638–644. [PubMed: 20096680]
18. McAleavey SA, Nightingale KR, Trahey GE. Estimates of echo correlation and measurement bias in acoustic radiation force impulse imaging. IEEE Trans Ultrason Ferroelectr Freq Control. Jun; 2003 50(6):631–641. [PubMed: 12839175]
19. Palmeri ML, McAleavey SA, Trahey GE, Nightingale KR. Ultrasonic tracking of acoustic radiation force-induced displacements in homogeneous media. IEEE Trans Ultrason Ferroelectr Freq Control. Jul; 2006 53(7):1300–1313. [PubMed: 16889337]
20. Nightingale, K.; Soo, MS.; Nightingale, R.; Bentley, R.; Stutz, D.; Palmeri, M.; Dahl, J.; Trahey, G. Acoustic radiation force impulse imaging: remote palpation of the mechanical properties of tissue. 2002 IEEE Ultrasonics Symposium, 2002. Proceedings; Munich, Germany. p. 1821-1830.
21. Mauldin FW, Viola F, Walker WF. Reduction of echo decorrelation via complex principal component filtering. Ultrasound Med Biol. Aug; 2009 35(8):1325–1343. [PubMed: 19520491]
22. Mauldin FW, Viola F, Walker WF. Complex principal components for robust motion estimation. IEEE Trans Ultrason Ferroelectr Freq Control. Nov; 2010 57(11):2437–2449. [PubMed: 21041131]
23. Walker WF, Trahey GE. A fundamental limit on delay estimation using partially correlated speckle signals. IEEE Trans Ultrason, Ferroelect, Freq Contr. Mar; 1995 42(2):301–308.
24. Nightingale K, Soo MS, Nightingale R, Trahey G. Acoustic radiation force impulse imaging: in vivo demonstration of clinical feasibility. Ultrasound Med Biol. Feb; 2002 28(2):227–235. [PubMed: 11937286]
25. Palmeri ML, Sharma AC, Bouchard RR, Nightingale RW, Nightingale KR. A finite-element method model of soft tissue response to impulsive acoustic radiation force. IEEE Trans Ultrason Ferroelectr Freq Control. Oct; 2005 52(10):1699–1712. [PubMed: 16382621]
26. Palmeri ML, McAleavey SA, Fong KL, Trahey GE, Nightingale KR. Dynamic mechanical response of elastic spherical inclusions to impulsive acoustic radiation force excitation. IEEE Trans Ultrason Ferroelectr Freq Control. Nov; 2006 53(11):2065–2079. [PubMed: 17091842]
27. Gallippi CM, Nightingale KR, Trahey GE. BSS-based filtering of physiological and ARFI-induced tissue and blood motion. Ultrasound Med Biol. Nov; 2003 29(11):1583–1592. [PubMed: 14654154]
28. Behler RH, Nichols TC, Zhu H, Merricks EP, Gallippi CM. ARFI imaging for noninvasive material characterization of atherosclerosis. Part II: toward in vivo characterization. Ultrasound Med Biol. Feb; 2009 35(2):278–295. [PubMed: 19026483]
29. Urban MW, Chen S, Greenleaf J. Harmonic motion detection in a vibrating scattering medium. IEEE Trans Ultrason Ferroelectr Freq Control. Sep; 2008 55(9):1956–1974. [PubMed: 18986892]
30. Jensen JA, Svendsen NB. Calculation of pressure fields from arbitrarily shaped, apodized, and excited ultrasound transducers. IEEE Trans Ultrason Ferroelectr Freq Control. 1992; 39(2):262–267. [PubMed: 18263145]
31. Torr GR. The acoustic radiation force. Am J Phys. 1984; 52(5):402.

32. Starritt HC, Duck FA, Humphrey VF. Forces acting in the direction of propagation in pulsed ultrasound fields. Phys Med Biol. Nov; 1991 36(11):1465–1474. [PubMed: 1754617]

33. Saad Y, Schultz MH. GMRES: A Generalized Minimal Residual Algorithm for Solving Nonsymmetric Linear Systems. SIAM Journal on Scientific and Statistical Computing. 1986; 7(3): 856.

34. Hackbusch, W. Multi-grid methods and applications. Springer; 1985.

35. Loupas T, Powers JT, Gill RW. An axial velocity estimator for ultrasound blood flow imaging, based on a full evaluation of the Doppler equation by means of a two-dimensional autocorrelation approach. IEEE Trans Ultrason, Ferroelect, Freq Contr. Jul; 1995 42(4):672–688.

36. Nightingale K, Palmeri M, Trahey G. Analysis of contrast in images generated with transient acoustic radiation force. Ultrasound Med Biol. Jan; 2006 32(1):61–72. [PubMed: 16364798]

37. Duck, FA. Physical properties of tissue: a comprehensive reference book. Academic Press; 1990.

38. Lediju M, Pihl M, Hsu S, Dahl J, Gallippi C, Trahey G. A motion-based approach to abdominal clutter reduction. IEEE Trans Ultrason, Ferroelect, Freq Contr. Nov; 2009 56(11):2437–2449.

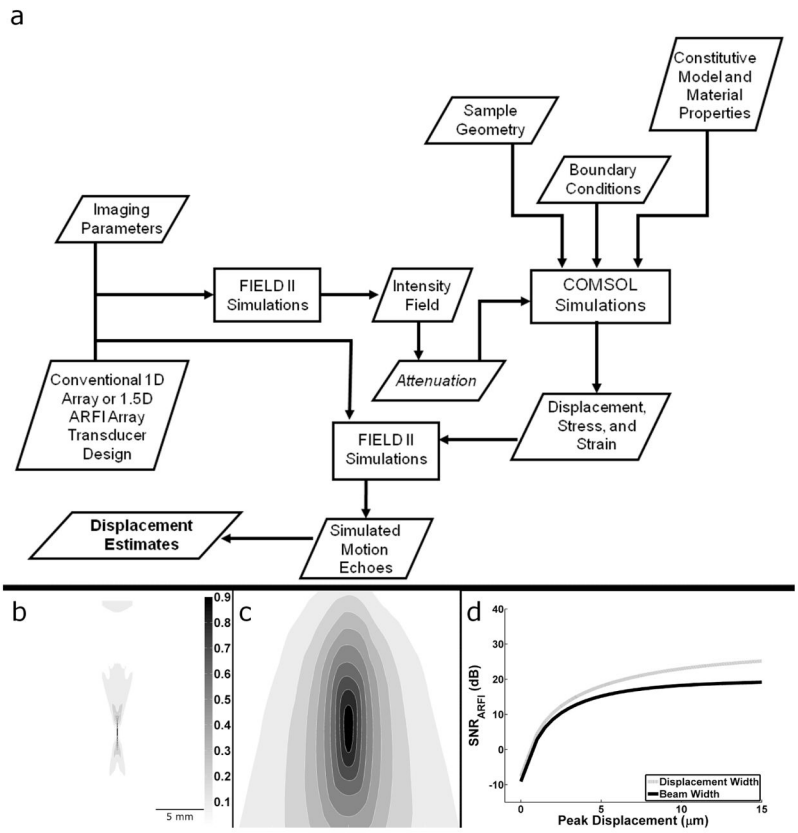

Fig. 1.

a) Block diagram of the numerical simulation framework. b) Intensity field output from FIELD II c) Displacement output from tissue FEM. Scale bar and color map of relative intensity apply to both images. d) Acoustic radiation force impulse SNR upper bound from (7) when using the actual displacement width parameter or the beam width proxy as in McAleavey *et al* [18].

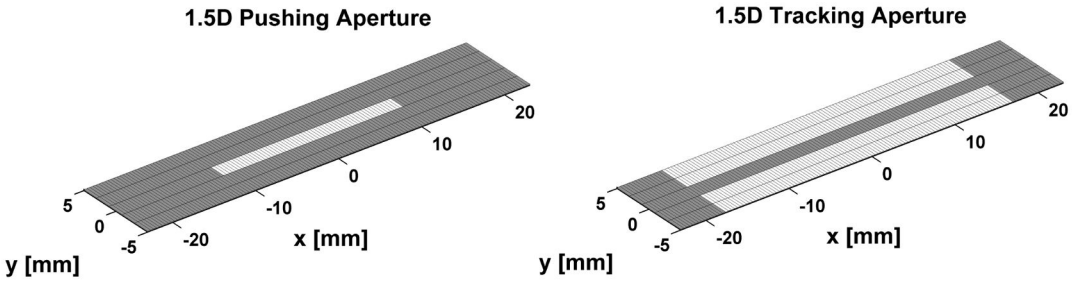

Fig. 2.

Pushing and tracking array geometry for the proposed 1.5D ARFI imaging transducer. White denotes active elements in the array.

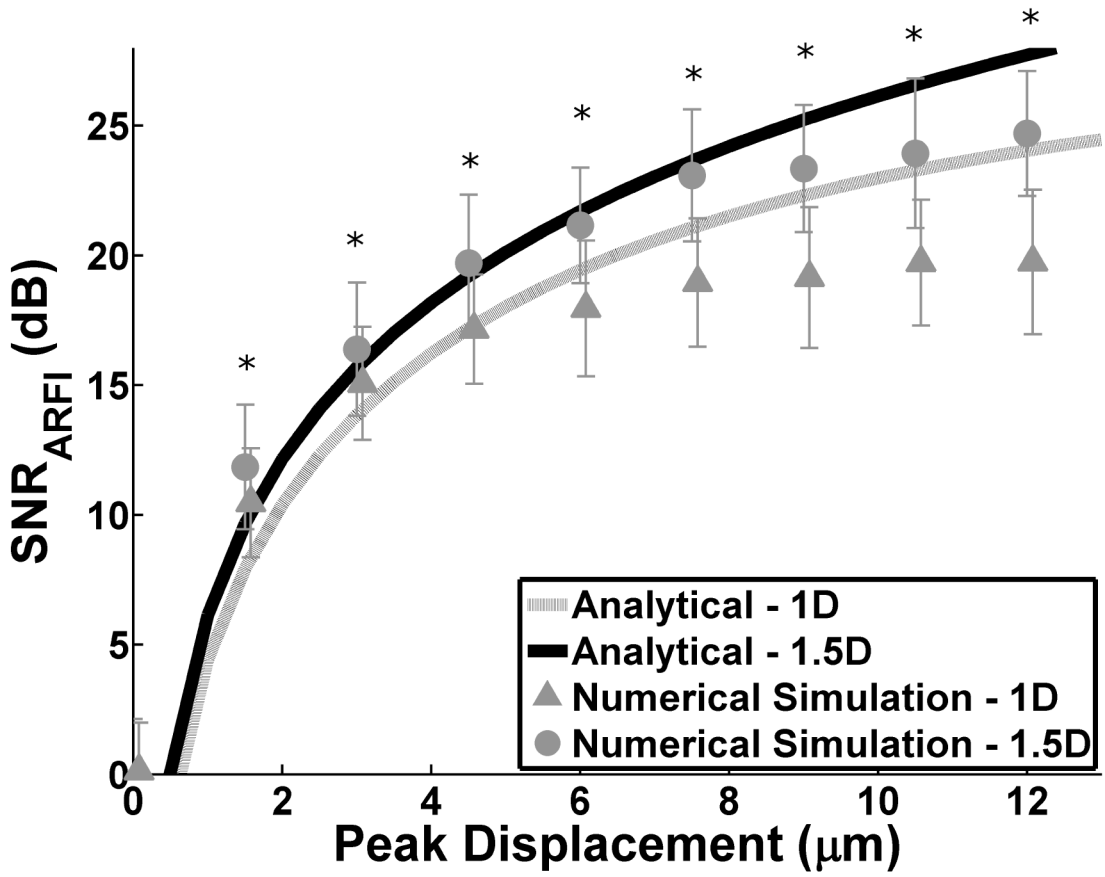

Fig. 3.

SNR_{ARFI} as a function of peak displacement. Solid lines represent the derived analytical model and the symbols with error bars are numerical simulation results for the 1D and 1.5D arrays. SNR_E = 30 dB. Mean and standard deviations for SNR_{ARFI} were calculated over 30 independent runs. * indicates significant difference between 1.5D and 1D numerical simulation (two sided t-test $p < 0.05$)

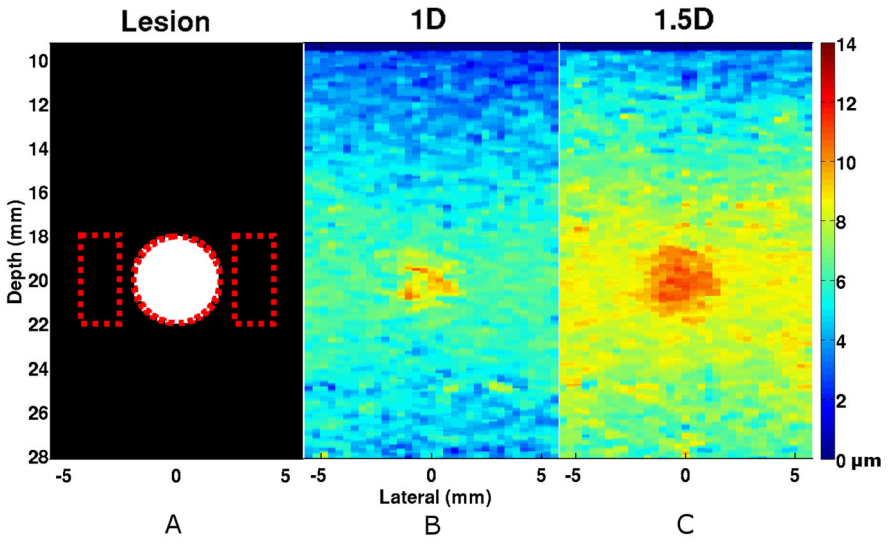

Fig. 4.

Simulated image of a compliant lesion embedded in stiffer surrounding tissue (1:10 ratio in Young's Modulus) imaged using either the (b) 1D or the (c) 1.5D array. The 1.5D array exhibited a 2.92 dB average improvement in CNR over the conventional 1D array (n=30). The (a) black and white image illustrates the location and size of the lesion (4 mm diameter, 20 mm depth) and the dotted lines indicate regions of interest (ROI) used for CNR and SNR calculations. Media-Color 1

Table I

Simulation parameters for the conventional 1D array and 1.5D ARFI array. With the exception of number of elements and center frequency, all other values were constant between the two designs in order to better compare the improvement in SNR_{ARFI} due to increased pushing to tracking beam width ratios.

	Conventional 1D		1.5D ARFI	
	Pushing	**Tracking**	**Pushing**	**Tracking**
Elements	60	96	60	4 × 96
Center Frequency (MHz)	4.21	6.15	2	7
Bandwidth (%)	50	80	50	80
Lateral Pitch (μm)	350			
Elevation Pitch (mm)	1			

Table II

Tissue displacement width, tracking beam width and the ratio of displacement width to tracking width (Disp, Track, Displ:Track, respectively) for the 1.5D ARFI and the conventional 1D array. The 1.5D ARFI array has a 9 fold increase in D_y and a 1.2 fold increase in D_x as compared to the conventional 1D array. For comparison, the ratio of pushing beam width to tracking beam width is also included.

Transducer	Direction	Displ (mm)	Track (mm)	Displ: Track (D_i)	Push:Track
Conventional 1D	Lateral	6.4	0.25	25.9	1.5
	Elevation	10.3	5.4	1.9	1.2
1.5D ARFI	Lateral	8.1	0.25	32.9	2.9
	Elevation	17.7	1.0	17.8	13.2

Table III

CNR and SNR values of the simulated lesion when imaged with the conventional 1D and the 1.5D ARFI array (n = 30). A 2.92 dB average improvement in CNR was achieved with the 1.5D ARFI array (two-sided t-test, $p < 0.0001$). The average SNR values inside and outside the lesion were also significantly improved with the 1.5D ARFI array ($p < 0.0001$).

Transducer	CNR (dB)	SNR_{lesion} (dB)	SNR_{tissue} (dB)
Conventional 1D	6.91±1.21	7.29±0.62	14.48±0.97
1.5D ARFI	9.82±0.83	11.02±0.68	23.26±1.64